ARTICLES

*Journal of Semiconductors*
(2020) 41, 072907
doi: 10.1088/1674-4926/41/7/072907

# Graphene plasmonic nanoresonators/graphene heterostructures for efficient room-temperature infrared photodetection

**Tian Sun[1], Weiliang Ma[1], Donghua Liu[2], Xiaozhi Bao[3], Babar Shabbir[6], Jian Yuan[4], Shaojuan Li[5], Dacheng Wei[2, †], and Qiaoliang Bao[6, †]**

[1]Wuhan National Laboratory for Optoelectronics and School of Optical and Electronic Information, Huazhong University of Science and Technology, Wuhan 430074, China

[2]State Key Laboratory of Molecular Engineering of Polymers, Department of Macromolecular Science, Fudan University, Shanghai 200433, China

[3]Joint Key Laboratory of the Ministry of Education, Institute of Applied Physics and Materials Engineering (IAPME), University of Macau, Macau, China

[4]School of Physics and Electronic Information, Huaibei Normal University, Huaibei 235000, China

[5]State Key Laboratory of Applied Optics, Changchun Institute of Optics Fine Mechanics and Physics, Chinese Academy of Sciences, Changchun 130033, China

[6]Department of Materials Science and Engineering, and ARC Centre of Excellence in Future Low-Energy Electronics Technologies (FLEET), Monash University, Clayton, Victoria 3800, Australia

**Abstract:** High-performance infrared (IR) photodetectors made by low dimensional materials promise a wide range of applications in communication, security and biomedicine. Moreover, light-harvesting effects based on novel plasmonic materials and their combinations with two-dimensional (2D) materials have raised tremendous interest in recent years, as they may potentially help the device complement or surpass currently commercialized IR photodetectors. Graphene is a particularly attractive plasmonic material because graphene plasmons are electrically tunable with a high degree of electromagnetic confinement in the mid-infrared (mid-IR) to terahertz regime and the field concentration can be further enhanced by forming nanostructures. Here, we report an efficient mid-IR room-temperature photodetector enhanced by plasmonic effect in graphene nanoresonators (GNRs)/graphene heterostructure. The plasmon polaritons in GNRs are size-dependent with strong field localization. Considering that the size and density of GNRs are controllable by chemical vapor deposition method, our work opens a cost-effective and scalable pathway to fabricate efficient IR optoelectronic devices with wavelength tunability.

**Key words:** graphene plasmons; nanoresonators; s-SNOM; mid-infrared photodetectors

**Citation:** T Sun, W L Ma, D H Liu, X Z Bao, B Shabbir, J Yuan, S J Li, D C Wei, and Q L Bao, Graphene plasmonic nanoresonators/graphene heterostructures for efficient room-temperature infrared photodetection[J]. *J. Semicond.*, 2020, 41(7), 072907. http://doi.org/10.1088/1674-4926/41/7/072907

## 1. Introduction

High-performance mid-infrared (mid-IR) photodetectors are widely used in security and biomedical areas[1, 2]. However, the commercialized infrared (IR) photodetectors are always operating with the cooling components with large volume and high cost[3]. Two-dimensional (2D) materials possessing extraordinary optical and electrical properties have emerged as promising candidates for highly efficient photodetection in the mid-IR frequency at room temperature[4–6]. Among the huge libraries of 2D materials, graphene attracted considerable attention in the past few years because of its unique electronic structures[7, 8]. The ultra-broadband photo-electric effect arising from the uniform light absorption spanning the range from ultraviolet to terahertz, made it to be the most appealing media for long-wavelength photodetection[9, 10]. However, the unique electronic properties of graphene are also accompanied by its gapless nature; leading to the huge dark current and relatively low photoresponsivity[11]. Although the significant progress on photodetectors using 2D materials (such as 2D transition metal dichalcogenides, TMDCs) and their heterostructures have been achieved in recent years[12, 13], photodetection in mid-IR range has been largely left behind due to the lack of suitable photoresponsive media as well as enhancement regime. To realise high-performance mid-IR photodetection, the material needs not only a narrow bandgap and decent carrier mobility but also desired photoabsorption at the mid-IR range[14]. A few operation mechanisms such as photovoltaic, photogating, thermoelectric and bolometric effects can contribute to the photocurrent generation in IR photodetectors, and usually two effects appear simultaneously[9, 15, 16]. It is noted that IR photodetectors based on thermoelectric and bolometric effects have relatively slow response and low photoresponsivity[17]. To improve the photoresponsivity and gain of the detectors, the photogating effect is a widely used way in 2D photoelectric devices. Although the local electric field induced by the incident photo can modulate the conductivity of the device then further improve the perform-

Correspondence to: D C Wei, weidc@fudan.edu.cn; Q L Bao, Qiaoliang.Bao@gmail.com

Received 7 JUNE 2020; Revised 27 JUNE 2020.

ance of the detectors, the intrinsic low quantum efficiency is still limited by the weak mid-IR light absorption[18, 19]. Only confining and capturing more mid-IR photons can essentially enhance the quantum efficiency. This brings up the question that how can we keep the property of broadband room temperature detection at mid-IR without sacrificing the quantum efficiency. The plasmonic media which can confine the electromagnetic field at nanoscale then modulate the photonic density of the state may effectively break the limitation in mid-IR photodetection based on 2D materials[20–22].

Controlling light at the sub-wavelength scale plays a pivotal role in a wide variety of areas ranging from physics and photonics to biology[23–25]. The sub-wavelength confinement of light requires the confining materials to have a negative permittivity[26]. For instance, the permittivity of noble metals remains negative in the visible range because of the large number of free electrons; thus, the collective oscillations of the electrons, referred to surface plasmons, can give rise to strongly enhanced optical near-fields confined in the metal[27]. However, the loss associated with electron/plasma scattering and interband transitions is unacceptably large[28, 29]. Graphene surface plasmon polaritons have the potential to bypass major hurdles associated with plasmons in metal nanostructures, such as the narrow spectral ranges (mainly visible and near-IR frequencies), poor field confinement at the mid-IR range and high optical losses inherent in metals[30–32]. Moreover, the electromagnetic field can be further concentrated by artificial nanostructures which will act as Fabry-Perot (F-P) nanoresonators for graphene plasmons[33–35]. However, their obvious damping channel during nanostructure fabrication (fabrication losses) may limit the development of graphene plasmon-based nanophotonic and nano-optoelectronic devices. To date, highly localized plasmonic modes in man-made nanostructures have been investigated by near-field and far-field experiments[34–37], however, the low-loss as-grown nanoresonators and their potentials for enhanced mid-IR photodetection have been largely unexplored.

Here, we demonstrated graphene-based mid-IR photodetector enhanced by the plasmonic effect from another layer of as-grown GNRs array. The array of GNRs was prepared by quasi-equilibrium plasma-enhanced chemical vapor deposition method, which is ultra-clean and size-controllable. We imaged the mid-IR "hot spot" in arrays by investigating the localized modes of graphene plasmon in individual GNRs using scattering-type scanning near-field optical microscopy (s-SNOM) in real space. Our study will shed new light on the efficient mid-IR light-harvesting device.

## 2. Experiment

### 2.1. Growth of GNRs and Fabrication of the device

GNRs were prepared by qe-PECVD. The details can refer to the Ref. [38]. We control the size and density of GNRs by the methane gas flow, the time and temperature of growth. The GNRs were directly obtained on the $SiO_2$/Si substrate. The GNRs/graphene heterostructure was fabricated by placing the PMMA-supported CVD graphene on top of the GNRs covered by thin layer h-BN. The devices were patterned by using the standard UV lithography. The electrodes are deposited with electron-beam evaporation.

### 2.2. s-SNOM set up

The mid-IR imaging described in the main text was performed using a commercial s-SNOM (Neaspec Company. Bunsenstr. 5 D-82152 Martinsried [Munich] Germany www.neaspec.com) equipped with a $CO_2$ laser (Access Laser Company. 917 134th St SW, Suite A1 Everett, WA 98204. www.accesslaser.com). The laser used here covers a wavelength range of 10.8–11.3 $\mu$m. The incident IR light is focused on the Pt-coated high-frequency oscillating AFM tip, and the tapping frequency and amplitude are approximately 270 kHz and 50 nm, respectively. The backscattered light is recorded via pseudo heterodyne detection, and the detected signal is then demodulated at the 3rd harmonic of the tip vibration frequency.

### 2.3. Simulation of graphene plasmons in GNRs

The numerical calculations were done in our work using the finite boundary elements method (commercial Comsol software). The graphene was defined as a two-dimensional conducting layer with the conductivity. The conductivity of graphene was modeled as random-phase approximation[35].

$$\sigma_{\text{intra}} = \frac{2ie^2t}{\hbar\pi(\alpha+i\gamma)}\ln\left[2\cosh\left(\frac{1}{2t}\right)\right],$$

$$\sigma_{\text{inter}} = \frac{e^2}{4\hbar}\ln\left[\frac{1}{2}+\frac{1}{\pi}\arctan\left(\frac{\alpha-2}{2t}\right)-\frac{i}{2\pi}\ln\frac{(\alpha+2)^2}{(\alpha-2)^2+(2t)^2}\right].$$

The $\alpha$, $\gamma$ and $t$ present the frequency, decay rate and temperature. By slightly tuning the value of decay rate, we can obtain the well agreement with the experiments.

## 3. Result and discussion

### 3.1. Graphene nano-disk characterizations

The graphene nano-disks were grown by the quasi-equilibrium plasma-enhanced chemical vapor deposition (qe-PECVD) system, which is illustrated in Fig. 1(a). The radio frequency plasma generator introduces the methane plasma into the quartz tube of the tubular furnace. The size and distribution of graphene nano-disks are highly controllable by tuning the factor during the growth process. The details of growth can be referred to as the former work[38]. After 6 min growth at 0.13 torr and 635 °C, the graphene nano-disks were directly obtained on the $Si/SiO_2$ substrate without further transfer, which will effectively avoid pollution during the transfer process. Considering of the fact that graphene nano-disks for mid-IR field enhancement actually act as IR nanoresonators, we will name our graphene nano-disks as GNRs here. The atomic force microscopy image shows the atomically clean surface of GNRs with different sizes. To quantitatively assess the size distribution of GNRs, we select a random area of 1 $\mu m^2$ which is imaged by AFM, as shown in Fig. 1(b). The GNRs in the target area have a diameter range from 80 to 220 nm. The diameter of 60% of GNR is around 150 nm (shown in Fig. 1(f)). The statistical distribution indicates the good uniformity of nano-disks. The Raman spectrum of GNRs is shown in Fig. 1(c), whereas the peak at 1350 and 1570 $cm^{-1}$ are attributed to the characteristic vibration bands (D and G band). Fig. 1(d) shows the high-resolution transmission elec-

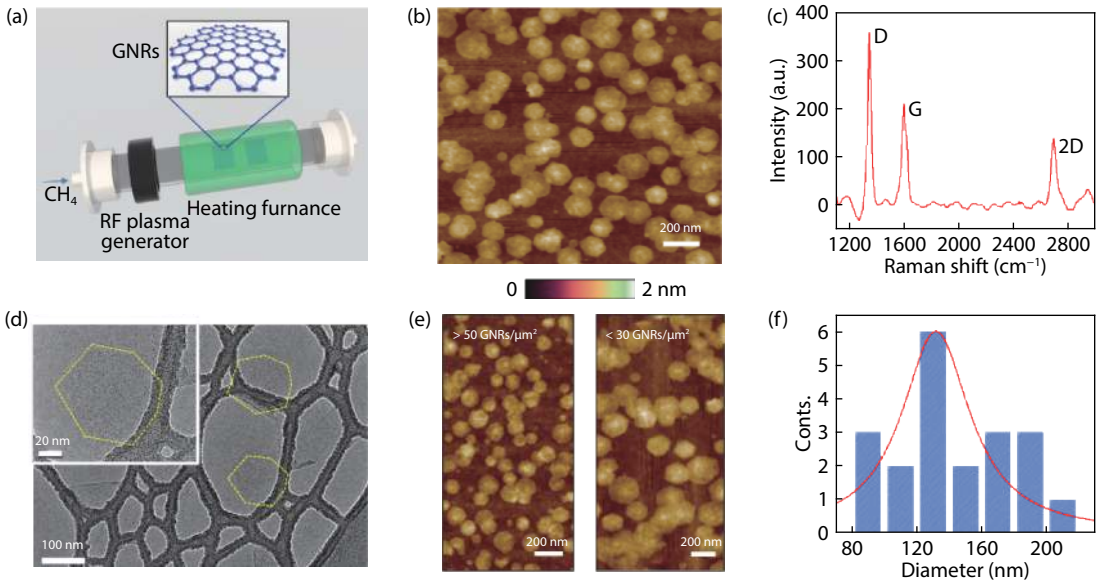


Fig. 1. (Color online) Characterization results of GNRs: AFM, HRTEM image and Raman spectrum, density and size distribution. (a) Representation of growth process of GNRs. The GNRs were obtained on the $SiO_2$/Si substrate by qe-PECVD. Upper image: Schematic illustration of the GNRs. (b) Atomic force microscope (AFM) image of GNRs. (c) The Raman spectrum shows the characteristic band (D, G, 2D) of GNRs. (d) A HRTEM image of GNRs. Scale bar: 100 nm. An enlarged HRTEM image. Scale bar: 20 nm. (e) The controlled density of GNRs, the AFM image indicate two different densities. Scale bar: 200 nm. (f) Statistical distribution of the diameter of GNRs with Gaussian fits overlaid.

tron microscopy (HRTEM) image of GNR. By tuning the growth time, growth temperature, and the power of the plasma generator, we can control the density of the GNRs. At the conditions of growth temperature $T$ = 635 ℃, growth time $t$ = 6 min, we can get the rough density of GNRs over 50 $\mu m^{-2}$. When increasing the temperature and growth time, the density decreases below 30 $\mu m^{-2}$ (as shown in Fig. 1(e)).

### 3.2. IR "hot spot" in GNRs

Over the past decade, graphene plasmon has received considerable attention for a wide range of applications especially in the technically important mid-IR to THz frequency ranges, such as in molecular sensors, terahertz detectors, and highly surface-enhanced Raman spectroscopy because of its ultrahigh confinement, facile processability and tunability via electric fields[8]. Among the various applications, surface plasmon "hot spots", which refer to the areas at sub-wavelength scale but with great local field enhancement caused by the near-filed coupling, play an important role. So the extremely high spatial resolution to resolve those "hot spots" is a prerequisite to study the plasmonic behavior of GNRs. Because of its high spatial resolution and ability to operate in the mid-IR range, s-SNOM is a powerful tool to image the real-space propagation and confinement characteristics of graphene plasmon[39].

Fig. 2(a) schematically illustrates the excitation of graphene plasmon in GNRs under s-SNOM. IR light (10.8–11.3 $\mu$m) is focused onto the Pt-coated high-frequency oscillating tip of an AFM. The tip also works as an optical antenna which launches a wave vector stronger than that of the incident light to match the excitation conditions of the graphene plasmon[30, 31]. The radius of curvature of the tip determines the spatial resolution of s-SNOM (approximately 25 nm). The polaritonic wave propagates in GNRs and is reflected by their edge. The reflected wave, after returning to the tip, interferes with the other local near-field signal, forming the periodic interference fringes. It should be noted that s-SNOM captures information from the local optical field underneath the tip. The propagating plasmon wave redistributes the surface near-field, and thus, we can extract the local intensities of GNRs directly from the amplitude of the local electrical field.

Fig. 2(b) shows the characteristic near-field amplitude $s(\omega)$ of GNRs at mid-IR. Several significant near-field features of GNRs can be observed: a bright spot in the center of small GNRs and a bright ring but a dark center in bigger GNRs. The different features indicate the various circular breathing modes in different GNRs[35]. Fig. 2(c) shows the relationship between the normalized amplitude at the center of GNR and the diameter of GNRs. An almost linear dependence of amplitude on the diameter of GNRs is observed. By tuning the excitation wavelength $\lambda_0$ from 10.69 to 10.78 $\mu$m, the two completely different breathing modes in the same GNR can be recognized (marked by a dashed white circle). Fig. 2(d) shows the line profiles of the normalized near-field amplitude $s(\omega)$ taken along the center span the circle in Fig. 2(b). Note that the near-field amplitude $s(\omega)$ is normalized to the $SiO_2$ substrate for quantitative analysis because of the approximately flat dispersion of $SiO_2$ in this frequency range. This result indicates that the graphene plasmon modes in GNRs are also closely related to the excitation wavelength.

For unravel the accurate relationship between the near-field distribution and diameter of GNRs as well as excitation wavelength. We simulated the excitation of surface plasmon in GNRs, and the results are depicted in Figs. 2(e) and 2(f). Here we present the simulated near-field distribution around the GNRs at fixed dipole positions, the dipole is located 25 nm above the center of single GNR. For the fixed excitation wavelength (as shown in Fig. 2(e)), the wavelength of graphene plasmon is also fixed. Here we can see the clear positive and negative near-field contrast. The diameter of GNRs in-

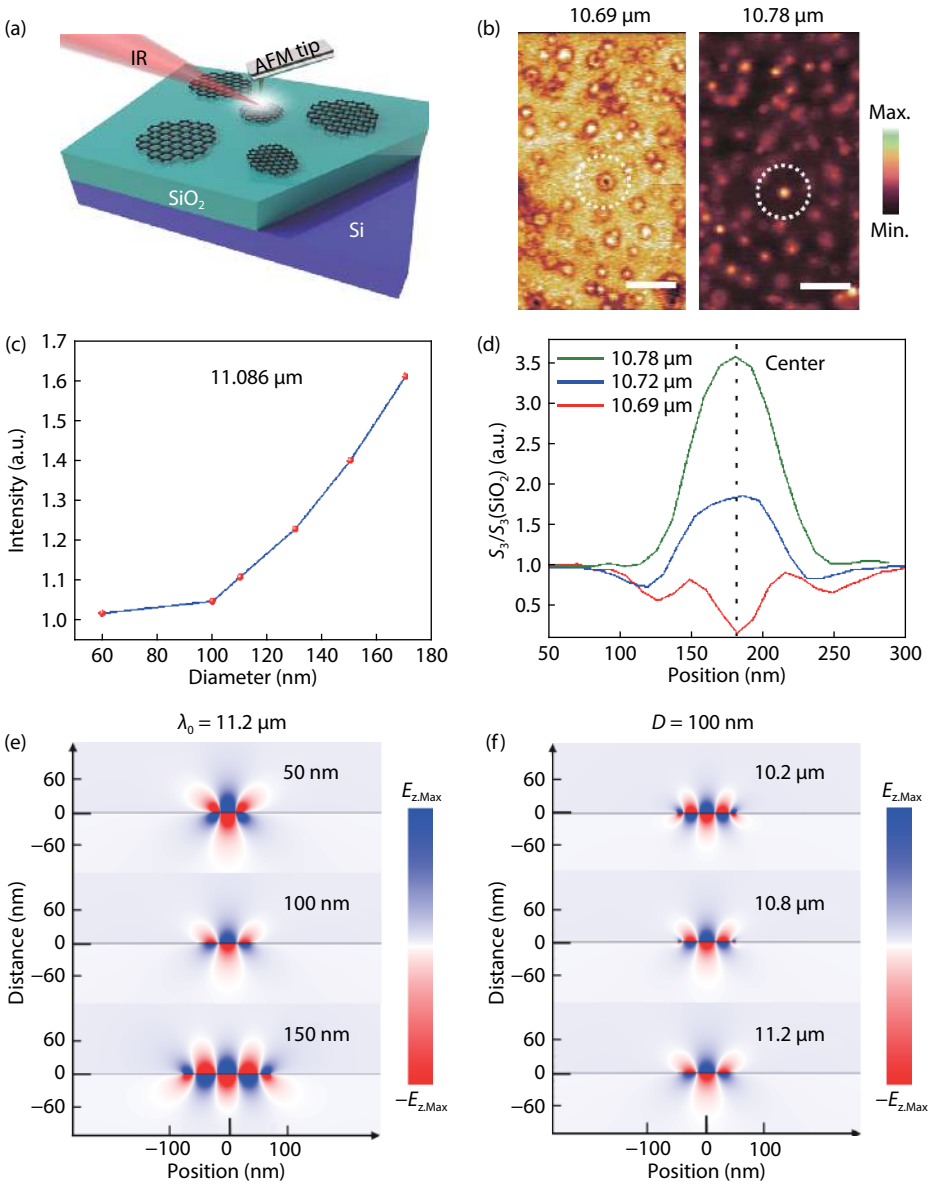


Fig. 2. (Color online) Schematics and mid-IR "hot-spot" of GNRs imaging with s-SNOM. (a) Simplified schematics of s-SNOM measurements: The Pt-coated tip is illuminated by mid-IR light and interacts with GNRs to launch and detect a graphene plasmon and their localized F-P modes in GNRs. (b) Near-field amplitude image of GNRs at $\lambda_0$ = 10.69 and 10.78 $\mu$m. The various "hot-spot" (localized graphene plasmon modes) in GNRs and clear wavelength dependence of modes in single GNR. (c) The center normalized near-field amplitude *s(ω)* shows strong dependence on the diameter of GNRs. The experimental points are all taken from the s-SNOM imaging. (d) Line profiles of the near-field amplitude *s(ω)* normalized to the $SiO_2$ substrate. The experimental profiles are taken from (b) (that is, all of these profiles are taken along the same line as shown in (b), indicating the graphene modes show strong dependence on excitation wavelength. (e) Calculated near-field distributions $E_z$ above the GNRs. The strong enhanced near-field $E_z$ shows dependence on diameter of GNR at $\lambda_0$ = 11.2 $\mu$m. (f) Calculated near-field distributions $E_z$ above the GNRs. The strong enhanced near-field $E_z$ indicates strong dependence on wavelength of incident mid-IR light at fixed diameter of GNR ($D$ = 100 nm).

fluences the near-field amplitude at the center and affects the graphene plasmon interference in the F-P cavity, which is GNR here. The longer excitation wavelength leads to less period of near-field distribution in GNRs with a fixed diameter (as shown in Fig. 2(f)), which suggests a linear relationship between $\lambda_{sp}$ and $\lambda_0$. The simulated results generally agree with our experimental observations (as shown in Figs. 2(b) and 2(d)) and also are consistent with previous work[35]. It is noteworthy that for all the simulated results, the strong near-field can still be found even above the GNRs 30 nm. This envisions the huge potential of GNRs for enhanced mid-IR light-matter interaction.

### 3.3. Room temperature mid-IR photodetector based on GNRs/graphene heterostructure

Considering the potential for enhanced light-matter interaction of GNRs, we combine the GNRs with pure monolayer graphene to fabricate GNRs/graphene vertical heterostructure for mid-IR photodetectors. Fig. 3(a) shows the optical image of the individual device in which the interdigitated antenna electrodes can efficiently help to capture more mid-IR light. As shown in Fig. 3(b), the schematic illustration of mid-IR photodetector based on GNRs/graphene heterostructure device are presented. The device structure comprises Ti/Au

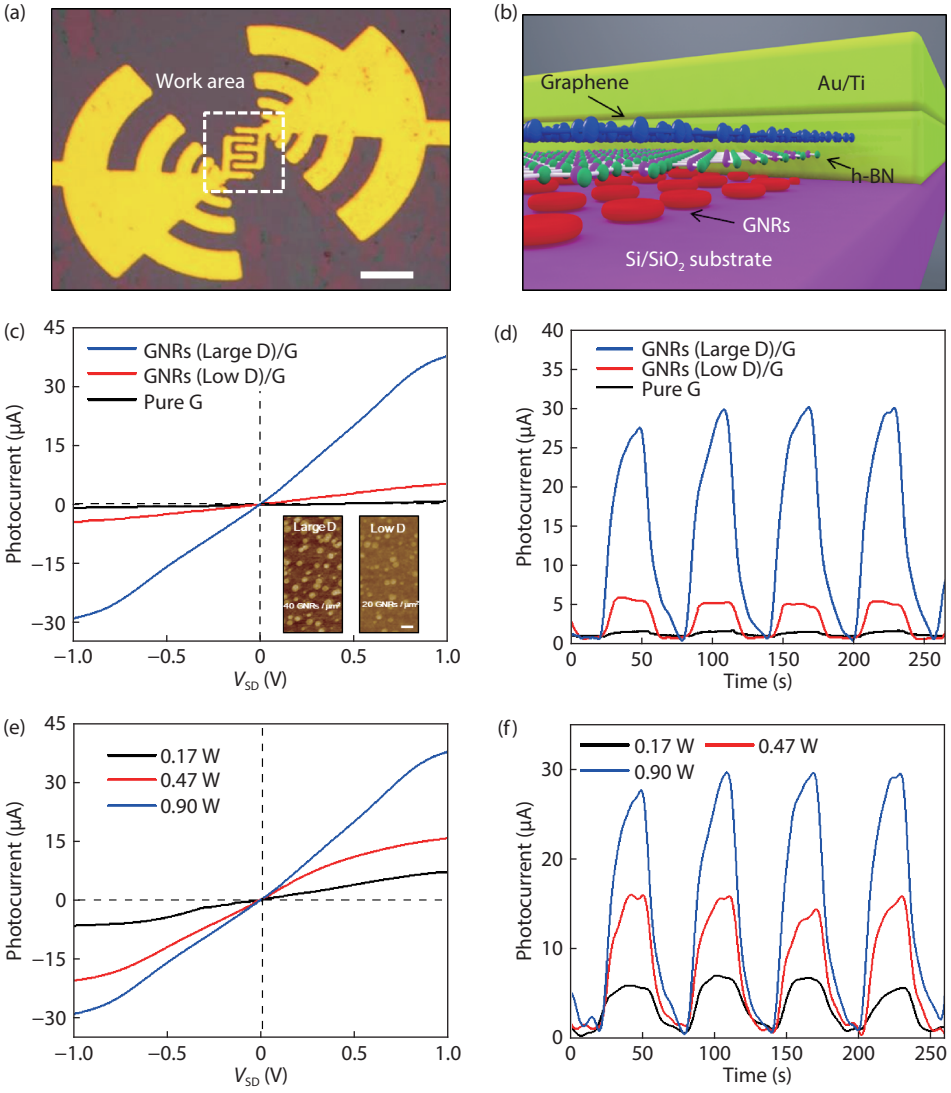


Fig. 3. (Color online) Room temperature mid-IR photodetector based on GNRs/graphene heterostructure. (a) Optical image of heterostructure mid-IR photodetector with efficient interdigitated antenna electrodes, Scale bar: 50 $\mu$m. (b) Schematic illustration of the mid-IR photodetector. All electrical measurement is conducted under 11.2 $\mu$m light illumination. (c) Dependence of photocurrent on source–drain voltage ($V_{SD}$) and (d) time-dependent photocurrent response ($V_{SD}$ = 1 V, $V_G$ = 0 V) for pure graphene photodetector (black), GNRs/G heterostructure photodetector with different GNRs density. Large D: large density > 40 GNRs/$\mu$m$^2$. Low D: low density < 20 GNRs/$\mu$m$^2$. Scale bar: 300 nm. Inset: AFM image of different GNRs density. GNRs/G: GNRs/graphene. (e) Photocurrent as the function of $V_{SD}$ with different incident power and (f) time-dependent photocurrent response for GNRs/G heterostructure photodetector with large GNRs density ($V_{SD}$ = 1 V, $V_G$ = 0 V).

(10 nm/100 nm) electrodes, GNRs, hexagonal boron nitride (h-BN), and monolayer graphene. A thin layer of h-BN (thickness: 2 nm) is sandwiched between graphene and GNRs as a dielectric layer and plays an important role to prevent non-equilibrium carriers from transferring between materials.

Fig. 3(c) plots the characteristic curves of photocurrent ($I_{ph} = I_{light} - I_{dark}$) versus bias voltage ($V_{SD}$) for pure graphene photodetector (black), GNRs/graphene heterostructure photodetector with different GNRs density. All the measurements were performed at room temperature. When IR light focused to a beam spot with a diameter of 1 cm is irradiated to the surface of the heterostructure, the electron-hole pairs are generated immediately in graphene film and collected by electrodes driven by an external electrical field. It is notable that the photocurrent in GNRs/graphene hybrid devices is much larger than that in pure graphene photodetector. Interestingly, the larger the density of GNRs in the heterostructure, the higher the photocurrent in the device. We conclude that graphene in this heterostructure absorbs more mid-IR light than pure graphene and more GNRs could help to localize more IR photons, thus increasing the absorption capacity in graphene. The inset of Fig. 3(c) shows the representative AFM image of GNRs with different densities. Fig. 3(d) shows the photocurrent changes periodically when switching on and off the incident laser at 10.6 $\mu$m and the photoresponse time is relatively long considering general thermal effect in IR radiation. For GNRs/graphene heterostructure photodetector with large GNRs density, the photocurrent as a function of $V_{SD}$ at different incident powers and time-dependent photocurrent response are shown in Figs. 3(e) and 3(f). The photocurrent increases almost linearly while $V_{SD}$ increases. It is worth pointing out that the photo response remains identical after several tens of switching cycles. The key figure-of-merit parameters of the device, responsivity ($R$), is

given by $R = I_{photocurrent}/P_{optical}$, where $P_{optical}$ is the illumination power in the work area of the device. When the incident power is 0.17 W, the responsivity of GNRs/graphene heterostructure photodetector is 1.73 A/W at $V_{SD}$ = 1 V, which is hundreds of time higher than that of pure graphene.

## 4. Conclusion

Our work investigated the plasmonic properties of as-grown graphene nano-disk GNRs and explored the mid-IR photodetection properties of GNRs/graphene heterostructure. By using IR nano-imaging techniques, we found that near-field confinement in GNRs shows a strong dependence on diameter and excitation wavelength. The performance of graphene mid-IR photodetector can be enhanced by incorporating GNRs to enhance the light absorption, and it can be further modulated by controlling the density of GNRs. Notably, our work envisions the huge potential of as-grown nanostructured graphene for photonic applications, which cover a broad range in the technologically important IR bands.

## Acknowledgement

We acknowledge support from the National Key Research & Development Program (No. 2016YFA0201902, 2018YFA0703200), Shenzhen Nanshan District Pilotage Team Program (LHTD20170006), National Natural Science Foundation of China (61974099 and 61604102, 51773041, 61890940), Shanghai Committee of Science and Technology in China (18ZR1404900), Natural Science Research Project for Anhui Universities (Grant No. KJ2019A0596), Youth Project of Provincial Natural Science Foundation of Anhui (Grant No. 2008085QF319) and Australian Research Council (ARC, FT150100450 and IH150100006).

## References

[1] Schneider H, Fuchs F, Dischler B, et al. Intersubband absorption and infrared photodetection at 3.5 and 4.2 $\mu$m in GaAs quantum wells. Appl Phys Lett, 1991, 58, 2234

[2] Naumann A, Navarro-González M, Peddireddi S, et al. Fourier transform infrared microscopy and imaging: Detection of fungi in wood. Fungal Genet Biol, 2005, 42, 829

[3] Lao Y F, Unil Perera A G, Li L H, et al. Tunable hot-carrier photodetection beyond the bandgap spectral limit. Nat Photonics, 2014, 8, 412

[4] Chen X L, Lu X B, Deng B C, et al. Widely tunable black phosphorus mid-infrared photodetector. Nat Commun, 2017, 8, 1672

[5] Freitag M, Low T, Zhu W J, et al. Photocurrent in graphene harnessed by tunable intrinsic plasmons. Nat Commun, 2013, 4, 1951

[6] Amani M, Regan E, Bullock J, et al. Mid-wave infrared photoconductors based on black phosphorus-arsenic alloys. ACS Nano, 2017, 11, 11724

[7] Lin Y M, Dimitrakopoulos C, Jenkins K A, et al. 100-GHz transistors from wafer-scale epitaxial graphene. Science, 2010, 327, 662

[8] Bao Q L, Loh K P. Graphene photonics, plasmonics, and broadband optoelectronic devices. ACS Nano, 2012, 6, 3677

[9] Vicarelli L, Vitiello M S, Coquillat D, et al. Graphene field-effect transistors as room-temperature terahertz detectors. Nat Mater, 2012, 11, 865

[10] Sensale-Rodriguez B, Yan R S, Kelly M M, et al. Broadband graphene terahertz modulators enabled by intraband transitions. Nat Commun, 2012, 3, 780

[11] Mueller T, Xia F N, Avouris P. Graphene photodetectors for high-speed optical communications. Nat Photonics, 2010, 4, 297

[12] Lopez-Sanchez O, Lembke D, Kayci M, et al. Ultrasensitive photodetectors based on monolayer $MoS_2$. Nat Nanotechnol, 2013, 8, 497

[13] Wang X D, Wang P, Wang J L, et al. Ultrasensitive and broadband $MoS_2$ photodetector driven by ferroelectrics. Adv Mater, 2015, 27, 6575

[14] Long M S, Wang P, Fang H H, et al. Progress, challenges, and opportunities for 2D material based photodetectors. Adv Funct Mater, 2019, 29, 1803807

[15] Rao G, Freitag M, Chiu H Y, et al. Raman and photocurrent imaging of electrical stress-induced p–n junctions in graphene. ACS Nano, 2011, 5, 5848

[16] Freitag M, Low T, Xia F N, et al. Photoconductivity of biased graphene. Nat Photonics, 2013, 7, 53

[17] Buscema M, Island J O, Groenendijk D J, et al. Photocurrent generation with two-dimensional van der Waals semiconductors. Chem Soc Rev, 2015, 44, 3691

[18] Zhou X, Hu X Z, Yu J, et al. 2D layered material-based van der Waals heterostructures for optoelectronics. Adv Funct Mater, 2018, 28, 1706587

[19] Huo N J, Konstantatos G. Recent progress and future prospects of 2D-based photodetectors. Adv Mater, 2018, 30, 1801164

[20] Knight M W, Sobhani H, Nordlander P, et al. Photodetection with active optical antennas. Science, 2011, 332, 702

[21] Fang Z Y, Liu Z, Wang Y M, et al. Graphene-antenna sandwich photodetector. Nano Lett, 2012, 12, 3808

[22] Ju L, Geng B S, Horng J, et al. Graphene plasmonics for tunable terahertz metamaterials. Nat Nanotechnol, 2011, 6, 630

[23] Atwater H A, Polman A. Plasmonics for improved photovoltaic devices. Nat Mater, 2010, 9, 205

[24] Anker J N, Hall W P, Lyandres O, et al. Biosensing with plasmonic nanosensors. Nat Mater, 2008, 7, 442

[25] Hillenbrand R, Taubner T, Keilmann F. Phonon-enhanced light–matter interaction at the nanometre scale. Nature, 2002, 418, 159

[26] Boltasseva A, Atwater H A. Low-loss plasmonic metamaterials. Science, 2011, 331, 290

[27] Novotny L, Hecht B. Principles of nano-optics. Cambridge: Cambridge University Press, 2009

[28] Khurgin J B, Boltasseva A. Reflecting upon the losses in plasmonics and metamaterials. MRS Bull, 2012, 37, 768

[29] Khurgin J B, Sun G. In search of the elusive lossless metal. Appl Phys Lett, 2010, 96, 181102

[30] Chen J N, Badioli M, Alonso-González P, et al. Optical nano-imaging of gate-tunable graphene plasmons. Nature, 2012, 487, 77

[31] Fei Z, Rodin A S, Andreev G O, et al. Gate-tuning of graphene plasmons revealed by infrared nano-imaging. Nature, 2012, 487, 82

[32] Ni G X, McLeod A S, Sun Z, et al. Fundamental limits to graphene plasmonics. Nature, 2018, 557, 530

[33] Fang Z Y, Wang Y M, Schlather A E, et al. Active tunable absorption enhancement with graphene nanodisk arrays. Nano Lett, 2014, 14, 299

[34] Yan H G, Low T, Zhu W J, et al. Damping pathways of mid-infrared plasmons in graphene nanostructures. Nat Photonics, 2013, 7, 394

[35] Nikitin A Y, Alonso-González P, Vélez S, et al. Real-space mapping of tailored sheet and edge plasmons in graphene nanoresonators. Nat Photonics, 2016, 10, 239

[36] Yang X X, Zhai F, Hu H, et al. Far-field spectroscopy and near-field optical imaging of coupled plasmon-phonon polaritons in 2D van der waals heterostructures. Adv Mater, 2016, 28, 2931

[37] Xu Q Y, Ma T, Danesh M, et al. Effects of edge on graphene plasmons as revealed by infrared nanoimaging. Light: Sci Appl, 2017, 6, e16204

[38] Liu D H, Chen X S, Hu Y B, et al. Raman enhancement on ultra-clean graphene quantum dots produced by quasi-equilibrium plasma-enhanced chemical vapor deposition. Nat Commun, 2018, 9, 193

[39] Chen X Z, Hu D B, Mescall R, et al. Modern scattering-type scanning near-field optical microscopy for advanced material research. Adv Mater, 2019, 31, 1804774